# We are IntechOpen, the world's leading publisher of Open Access books Built by scientists, for scientists

6,900
Open access books available

185,000
International authors and editors

200M
Downloads

Our authors are among the

154
Countries delivered to

TOP 1%
most cited scientists

12.2%
Contributors from top 500 universities




WEB OF SCIENCE™

Selection of our books indexed in the Book Citation Index in Web of Science™ Core Collection (BKCI)

## Interested in publishing with us?
## Contact book.department@intechopen.com

Numbers displayed above are based on latest data collected.
For more information visit www.intechopen.com



Chapter 1

# Density Functional Perturbation Theory to Predict Piezoelectric Properties

Kaoru Nakamura, Sadao Higuchi and Toshiharu Ohnuma

Additional information is available at the end of the chapter

http://dx.doi.org/10.5772/intechopen.76827

**Abstract**

Among the various computational methods in materials science, only first-principles calculation based on the density functional theory has predictability for unknown material. Especially, density functional perturbation theory (DFPT) can effectively calculate the second derivative of the total energy with respect to the atomic displacement. By using DFPT method, we can predict piezoelectric constants, dielectric constants, elastic constants, and phonon dispersion relationship of any given crystal structure. Recently, we established the computational technique to decompose piezoelectric constants into each atomic contribution, which enable us to gain deeper insights to understand the piezoelectricity of material. Therefore, in this chapter, we will introduce the computational framework to predict piezoelectric properties of polar material by means of DFPT and details of decomposition technique of piezoelectric constants. Then, we will show some case studies to predict and discover new piezoelectric material.

**Keywords:** density functional perturbation theory, ferroelectricity, piezoelectricity, first-principles calculation

## 1. Introduction

In this chapter, we will introduce how recent computational techniques can successfully predict response properties, represented as piezoelectricity, by means of perturbation method. Piezoelectricity is the polarization change in response to external mechanical force. Inversely, if electrical field is applied to piezoelectric material, mechanical strain is induced (inverse piezoelectric effect). Therefore, piezoelectric materials are widely used as vibrational censors,

IntechOpen

© 2018 The Author(s). Licensee IntechOpen. This chapter is distributed under the terms of the Creative Commons Attribution License (http://creativecommons.org/licenses/by/3.0), which permits unrestricted use, distribution, and reproduction in any medium, provided the original work is properly cited. CC BY

surface acoustic wave devices, and actuators. Only the material having no inversion symmetry shows piezoelectricity. For example, **Figure 1** shows schematic illustration of the piezoelectric effect. Positions of positively charged ion (cation) and negatively charged ion (anion) are represented as plus and minus symbols. **Figure 1a** shows the paraelectric phase, where ions are orderly located with inversion symmetry. On the other hand, ions are slightly displaced by δ with respect to those in paraelectric phase, as shown in **Figure 1b**. Such small displacement induces microscopic polarization $P_s$ along the ionic displaced direction.

Because ferroelectric phase is energetically more stable than paraelectric phase under low temperature, $P_s$ is frequently referred as the spontaneous polarization. Above Curie temperature, ferroelectric properties are disappeared since paraelectric phase becomes more stable than ferroelectric one. **Figure 1c** shows the schematic illustration of the principal of piezoelectricity, where external stress (red-colored arrows) increases the ionic displacement and resultant polarization. In this case, external stress increases the spontaneous polarization by $\Delta P_s = P_s' - P_s$. Therefore, piezoelectric constant is defined as the derivative of the spontaneous polarization with respect to the external field. More detailed and comprehensive description of piezoelectricity is reviewed by Martin [1].

First-principles calculation based on density functional theory (DFT [2, 3]) has been widely utilized as the computational method to predict the electronic properties of material under the ground state. Ideally, required information to conduct the first-principles calculation is only the crystal structure, including atomic species and position of periodic/nonperiodic structure unit. The most significant advantage of first-principles calculation is its predictability. Since King-Smith and Vanderbilt showed the theoretical methodology to calculate change in polarization per unit volume $\Delta P$ [4], dielectric and piezoelectric properties of wide range of materials in which electronic correlations are not too strong [5–7] have been accurately predicted. The derivative of total energy determines various properties. For example, determined forces, stresses, dipole moment (first-order derivatives), dynamical matrix, elastic constants, dielectric and piezoelectric constants (second-order derivative), nonlinear dielectric susceptibility, phonon–phonon interaction and Grüneisen parameters (third-order derivative), and

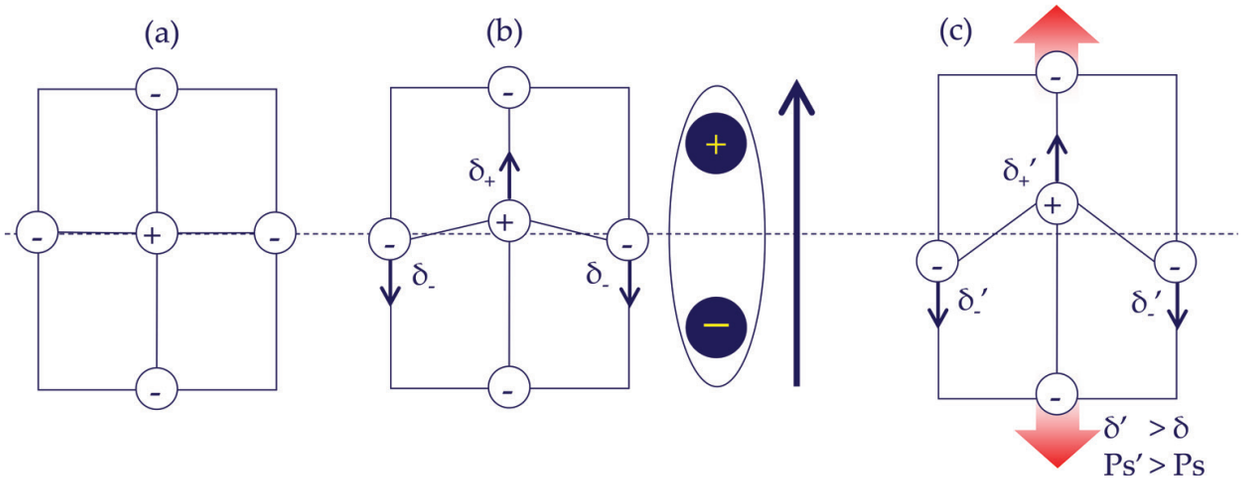



**Figure 1.** Ionic configuration of (a) paraelectric phase and (b) ferroelectric phase. (c) Ionic displacement according to the external force.

so on. Thus, first-principles calculation has been made use of calculating the perturbed total energy of materials because of its accuracy. Although perturbations were made by hand up to the early 1980s, sophisticated methodology of density functional perturbation theory (DFPT) was proposed in 1987 by Baroni et al. [5]. They showed general formulation of total energy change with respect to atomic displacement and opened the way to efficiently compute the energy derivative with respect to the perturbation [5]. DFPT can compute response properties directly arising from the perturbations of strain, atomic displacement, and electric field by making use of linear response theory [8–11]. Numbers of ferroelectric materials are theoretically investigated on the origin of their ferroelectric properties (including piezoelectricity and dielectric properties) by using DFPT. Because of technological importance, such theoretical researches have been focused on Pb-based perovskite material (e.g., $PbTiO_3$, $PbZrO_3$, and their solid solution [12–15]) because they have excellent piezoelectric properties and are widely applied for actuators. However, due to the restriction of hazardous substance (RoHS) directive, researches on lead-free ferroelectric materials have gathered great attraction. By taking advantage of the predictability of DFPT, various lead-free ferroelectric oxide and nitride materials were theoretically investigated on their piezoelectric properties [16–25]. Moreover, DFPT calculations showed that piezoelectricity can be greatly enhanced by imposing isotropic stress for $PbTiO_3$ [26, 27], uniaxial stress for $SrHfO_3$ [28], uniaxial and biaxial strain for AlN-GaN solid solution alloy [29], and two-dimensional epitaxial strain for doped ZnO [30]. As latterly explained, those enhancements of piezoelectric constant are thought to be closely related to the phase transition. In the next section, we will show the definition of piezoelectric constants within the framework of DFPT.

## 2. Formulation of piezoelectric constants

Formulation and calculation methodologies to obtain response properties of materials in the framework of DFPT have been developed in a step-by-step manner, because degrees of freedom by perturbations of atomic displacement, homogeneous electric fields, and strain are often strongly coupled. For example, piezoelectricity affects elastic and dielectric properties. Therefore, special care must be paid for the calculation of coupled properties. In 2005, Hamann et al. demonstrated that elastic and piezoelectric tensors can be efficiently calculated by treating homogeneous strain within the framework of DFPT [31]. At the same time, Wu et al. systematically formulated response properties with respect to displacement, strain, and electric fields [32]. In this section, we will briefly introduce how piezoelectric properties are formulated in the framework of DFPT. In each formulation, Einstein implied-sum notation is used. Cartesian directions $\{x, y, z\}$ are represented as $\alpha$ and $\beta$. Subscription of $j$ and $k = 1, \ldots, 6$ is the standard Voigt notation (represents directions of $xx$, $yy$, $zz$, $yz$, $zx$, and $xy$). The subscripts $m$ and $n$ are the degrees of freedom in the cell. They range from 1 to $3i$, where $i$ is the number of irreducible atoms because each atom has three degree of freedom along $x$, $y$, and $z$ directions.

Total energy of material under perturbation of atomic displacement $u$, electric field $\sigma$, and strain $\eta$, $E(u,\sigma,\eta)$, is defined as follows:

$$E(u, \sigma, \eta) = \frac{1}{\Omega_0}[E^0 - \Omega\sigma \cdot \mathrm{P}] \tag{1}$$

where $E^0$ is the total energy of material under the ground state, $\Omega_0$ is volume of the unit cell (smallest repeat unit of crystal), $\Omega$ is deformed volume of the unit cell, and P is the electric polarization. Following response functional tensor can be obtained by second-order differential of Eq. (1):

$$\text{Force constant matrix}: K_{mn} = \Omega_0 \frac{\partial^2 E}{\partial u_m \partial u_n}\bigg|_{\sigma,\eta} \tag{2}$$

$$\text{Clamped} - \text{ion term of electric susceptibility}: \bar{\chi}_{\alpha\beta} = -\frac{\partial^2 E}{\partial \sigma_\alpha \partial \sigma_\beta}\bigg|_{u,\eta} \tag{3}$$

$$\text{Clamped} - \text{ion term of elastic tensor}: \bar{C}_{jk} = -\frac{\partial^2 E}{\partial \eta_j \partial \eta_k}\bigg|_{u,\sigma} \tag{4}$$

$$\text{Born effective charge tensor}: Z_{m\alpha} = -\Omega_0 \frac{\partial^2 E}{\partial u_m \partial \sigma_\alpha}\bigg|_{\eta} \tag{5}$$

$$\text{Force} - \text{response internal} - \text{strain tensor}: \Lambda_{mj} = -\Omega_0 \frac{\partial^2 E}{\partial u_m \partial \eta_j}\bigg|_{\sigma} \tag{6}$$

$$\text{Clamped} - \text{ion piezoelectric tensor}: \bar{e}_{\alpha j} = \frac{\partial^2 E}{\partial \sigma_\alpha \partial \eta_j}\bigg|_{u} \tag{7}$$

Clamped-ion term is a frozen quantity, which indicates that atomic coordinates are not allowed to relax as the homogeneous electric field or strain. Therefore, dynamical term should be added into the clamped-ion term in order to obtain proper response properties.

Simplest and physically well-understandable piezoelectric constant can be expressed as follows:

$$e_{\alpha j} = \frac{\partial P_\alpha}{\partial \eta_j} \tag{8}$$

In this expression, it is easily understood that piezoelectric $e$ constant $e_{\alpha j}$ is a measure of the change in polarization induced by the external strain. As the atomic positions are changed according to the strain, change of the polarization includes both electronic contribution (clamped-ion term) and dynamical contribution (internal-strain term). The internal-strain term of piezoelectric constant is represented as follows:

$$\hat{e}_{\alpha j} = \frac{1}{\Omega_0} Z_{m\alpha} (K^{-1})_{mn} \Lambda_{nj} \tag{9}$$

Thus, proper piezoelectric constant can be obtained by Eqs. (7) and (9):

$$e_{\alpha j} = \left.\frac{\partial^2 E}{\partial \sigma_\alpha \partial \eta_j}\right|_u + \frac{1}{\Omega_0} Z_{m\alpha} (K^{-1})_{mn} \Lambda_{nj} \tag{10}$$

Here, the first and second terms on the right-hand side in Eq. (10) are the clamped-ion term and internal-strain term, respectively. The former shows the electronic contribution ignoring the atomic relaxation effect, and the latter shows the ionic contribution including the response of the atomic displacement to the strain. The Born effective charge $Z_{m\alpha}$, force-constant matrix $K_{mn}$, and internal-strain tensor $\Lambda_{nj}$ are the second derivatives of the energy with respect to the displacement and electric field, pairs of displacements, and displacement and strain, respectively. The internal-strain term of the piezoelectric stress constants can be further decomposed into the individual atomic contributions when the above second-derivative tensors are fully obtained.

On the other hand, the internal-strain term of the piezoelectric stress constant $e_{\alpha j}$ is frequently described by the following equation, using the Born effective charge $Z_{\alpha\beta}$ and displacement $u_\beta$ of each atom in the calculation cell:

$$\hat{e}_{\alpha j} = Z_{\alpha\beta} \frac{\partial u_\beta}{\partial \eta_j} \tag{11}$$

where $\partial u_\beta / \partial \eta_j$ shows the response of the first-order atomic displacement to the first-order strain. In this expression, the meaning of the piezoelectric stress constant, i.e., $e_j$ is a measure of the change in polarization induced by the external strain, is much more visible than in Eq. (9). In the DFPT formalism, $\partial u_\beta / \partial \eta_j$ is implicitly calculated as a displacement-response internal-strain tensor $\Gamma$ as follows [32]:

$$\Gamma_{nj} = \Lambda_{mj} (K^{-1})_{mn} \tag{12}$$

Because the subscript $n$ in $\Gamma_{nj}$ indicates the degrees of freedom, $\Gamma_{nj}$ can be decomposed into the individual atomic components, which also enables to calculate individual contribution of each atom for total piezoelectric constant.

Here, piezoelectric $e$ constant defined as Eq. (9) is frequently referred as "piezoelectric strain constant." On the other hand, it is much more natural and easy to control the stress (electric field) than to control the strain in any case. In this case, the piezoelectric strain constant $d_{\alpha j}$ is usually measured. It can be obtained from piezoelectric strain constant $e_{\alpha j}$ using the following relation:

$$d_{\alpha j} = s_{jk} e_{\alpha k} \tag{13}$$

where $s_{jk}$ is the elastic compliance, which is given by the inverse matrix of the elastic constants $C_{\mathrm{jk}}$.

Those formulations are implemented in specific first-principles simulation packages such as ABINIT [33] and Vienna ab initio simulation package (VASP) [34], and piezoelectric constants can be calculated on a daily basis. From the next section, we will show how DFPT calculation precisely gives piezoelectric properties of ferroelectric materials.

## 3. Introduction of target material

In this chapter, we selected $LiNbO_3$ as a target material to show the predictability of DFPT calculation. $LiNbO_3$ is one of ferroelectric materials and widely used as surface acoustic wave (SAW) and optical waveguide elements. Crystal structure of $LiNbO_3$, which belongs to the space group of *R3c*, is frequently referred as "strained perovskite structure." Schematic illustrations of crystal structure of $ABO_3$ perovskite and $LiNbO_3$ are shown in **Figure 2**.

Crystal structures shown in the present chapter was visualized by using VESTA software [35]. Curie temperature of $LiNbO_3$ is quite high and ranges from 1140 [36] to 1210°C dependent on the quality of sample (variation of Li/Nb relation can shift Curie temperature [37]). Below Curie temperature, ferroelectric phase with *R3c* symmetry (crystal structure can be classified into 230 types of space group according to the symmetry group) shown in **Figure 2a** is stable. Paraelectric phase with $R\bar{3}c$ symmetry, shown in **Figure 2b**, becomes stable above Curie temperature. In the paraelectric phase, it can be seen that both Li and oxygen is positioned with

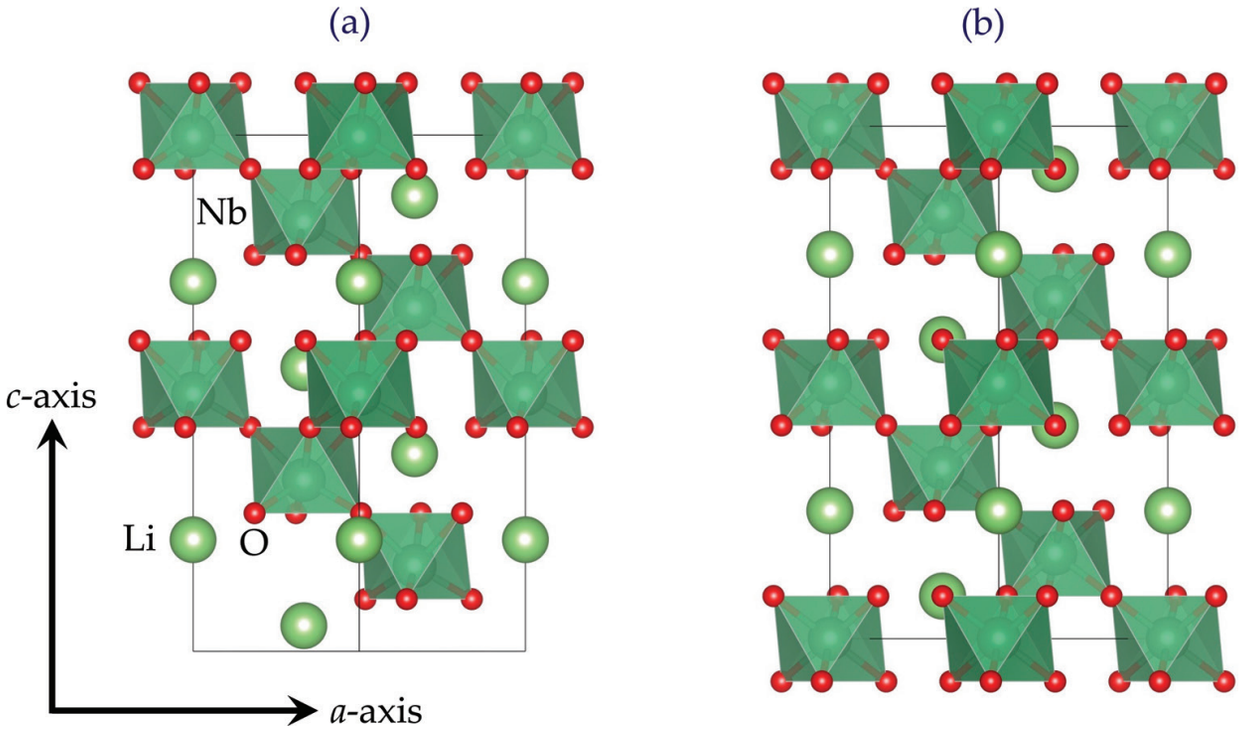



**Figure 2.** Crystal structures of (a) ferroelectric phase with *R3c* symmetry and (b) paraelectric phase with $R\bar{3}c$ symmetry $LiNbO_3$. Yellow green-, green-, and red-colored balls represent Li, Nb, and oxygen atoms, respectively. Bonding structures between Nb and surrounding oxygen atoms are represented as green-colored polyhedron. Two orthogonal crystallographic directions are shown as both *a*- and *c*-axes.

the same height along *c*-axis, and the position of Nb is just the center between two oxygen layers along *c*-axis. On the other hand, both Li and Nb are shifted in ferroelectric *R3c* phase along downward direction of *c*-axis with respect to those in paraelectric $R\bar{3}c$ phase.

Due to the different bonding nature between Li-O and Nb-O, atomic positions of Li and Nb are off-centered within oxygen layers along *c*-axis. This structural characteristic is the ferroelectric nature of $LiNbO_3$. One of the notable properties of $LiNbO_3$ is its high-curie temperature (~1400 K). However, piezoelectric properties of $LiNbO_3$ are not so much superior as compared with Pb-based perovskites. Crystal structure of piezoelectric $ABO_3$ perovskite is based on the cubic structure (of *Pm3m* symmetry), shown in **Figure 3a**.

Cubic lattice is symmetric and usually high-temperature phase, same as $LiNbO_3$. The "strained perovskite structure" expression for $LiNbO_3$ means that $LiO_6$ and $NbO_6$ polyhedron are largely rotated with respect to the cubic perovskite structure. However, because of the simple atomic configuration of cubic structure, atoms can be displaced along various directions and change crystalline symmetry as shown in **Figure 3a**. Crystalline lattice is vibrated (referred as phonon) under finite temperature. Some lattice vibrations along specific directions are unstable. This specific phonon is called as soft mode with imaginary frequency. In such case, atoms are displaced along unstable phonon mode to lower the total energy. For example, cooperative atomic displacement along [001] direction shown in **Figure 3b** (referred as $\Gamma_{15}$ mode) changes symmetry from cubic to tetragonal (of *P4mm* symmetry), which leads polarization along [001] direction. Thus, polarization direction of perovskite is not restricted and allowed to be changed. This characteristic rotational polarization direction is favorable for piezoelectricity because grains in polycrystalline material are oriented along various directions. Thus, careful controlling of crystal structure is essential to obtain superior piezoelectric properties.

The most convenient way to control and drastically change the crystal structure is imposing high pressure. Many compounds have found to be possible to form $LiNbO_3$-type structure under the high-pressure synthesis [38], and some of them were quenchable phase. For example, $LiNbO_3$-

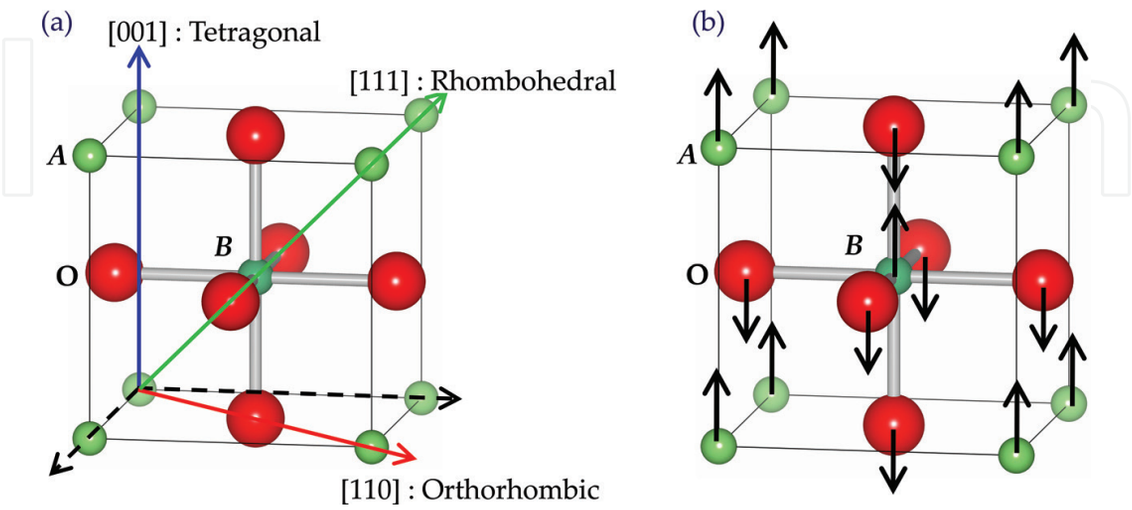



**Figure 3.** (a) Crystal structure of cubic $ABO_3$ perovskite and possible polarization directions. (b) Representative unstable vibrational mode of cubic $ABO_3$ perovskite showing as arrows.

type structured $ZnSbO_3$ was successfully synthesized [39] under high pressure, and improvement of the spontaneous polarization is suggested by enhancement of the covalency of Sn site from first-principles simulation [40]. Moreover, high-pressure synthesized research on $LiNbO_3$-type structure is now extended to more complex compounds such as oxynitrides [41, 42].

The crystal structure of $ABO_3$ compound is generally determined by the balance between the ionic radius of *A* and *B* element, which is frequently referred as tolerance factor. Due to the small size of the Li ion with respect to the tolerance factor of $LiNbO_3$, this compound cannot form stably the popular perovskite structure under the ambient condition. On the other hand, we predicted the crystal structures of high-pressure phase of $LiNbO_3$ [43], which were not completely elucidated by experimental study [44]. Revealed structures are $NaIO_3$-type structure (*Pnma*) as room temperature high-pressure phase and apatite-like structure ($P6_3/m$) as high-temperature high-pressure phase. It should be noted that the $NaIO_3$-type structure is closely related with the popular $GdFeO_3$-type perovskite structure. The only difference between these structures is that A-site position and B-site position are inter-exchanged. Therefore, there seems to be a possible way to connect the perovskite structure and $LiNbO_3$-type structure.

In our previous theoretical study on high-pressure phase, analysis was mainly concerned with phase transition mechanism only from the viewpoint of subgroup symmetry and energy barrier [43]. It will be instructive to deal with this phase transition phenomenon from the viewpoint of lattice instability as discussed in the field of the ferroelectric instability analysis. In the following section, we will show investigation on the potential piezoelectric properties of $LiNbO_3$ with various hypothetical crystal structures by the method of DFPT, and possible phase transition mechanism will be discussed from the viewpoint of soft mode.

## 4. Computational methodology

First-principles calculation was performed by using VASP code [34]. Interactions between ion and electron were treated by projector augmented wave (PAW) method [45]. PBEsol functional [46] was used to approximate exchanges and correlate interactions of electrons, which can be used to reproduce the lattice constants of various materials [45]. Precise calculation on the lattice constant is essential to predict piezoelectric properties because they depend on volume of unit cell Ω as shown in Eq. (1). The kinetic energy cutoff for plane waves was set at 500 eV, and the k-point mesh was set at ~0.03/Å intervals to obtain the converged total energy at less than 0.1 meV/atom. Before calculating the piezoelectric constants, atomic positions and cell parameters were optimized until the forces on each atom and cell converged at below $5 \times 10^{-4}$ eV/Å.

Since VASP does not directly calculate Eq. (12), we added routine to calculate displacement-response internal-strain tensor $\Gamma_{nj}$ and decompose piezoelectric constants into each atom. The sum of the decomposed piezoelectric constants was confirmed to accurately reproduce the total piezoelectric constants. Careful convergence tests with a higher energy cutoff and denser *k*-point mesh showed that the numerical accuracy of the calculated $\Gamma_{nj}$ was less than 0.01. It was confirmed that this error does not influence our discussion and conclusion. Moreover, it was confirmed that the values of $\Gamma_{nj}$ obtained by the DFPT method were consistent with those

calculated by the direct method, in which the strain-displacement relation of each ion was explicitly calculated.

On the basis of cubic *Pm3m* phase, lattice instability analysis was performed by phonon calculation utilizing phonopy code [47]. Force constant matrix shown in Eq. (2) was constructed by DFPT calculation implemented in VASP code combined with supercell approach. Supercell was constructed by using unit cell so that orthogonal three axes of the supercell exceed 10 Å. Note that although supercell is not required in DFPT approach, the present VASP code implements perturbation at the zone center.

## 5. Calculated piezoelectric properties of $LiNbO_3$

Calculated piezoelectric properties of $LiNbO_3$ in ferroelectric phase are summarized in **Table 1**. Some experimentally measured values are also shown in **Table 1**. All properties are confirmed to be well reproduced by calculation. In a technological importance, 33 components are the most important because *C*-axis of $LiNbO_3$ is polarization direction. Calculated values of $e_{33}$, $C_{33}$, and $\varepsilon_{33}$ are especially well reproduced. It should be mentioned here that chemical composition of $LiNbO_3$ used for experiment is congruent and includes Li vacancy. On the other hand, calculation was performed by using stoichiometric $LiNbO_3$.

| | **Calculated value** | **Experimental value** |
|---|---|---|
| Piezoelectric stress constant ($C/m^2$) | | |
| $e_{15}$ | 3.73 | 3.655 ± 0.022 [48], 3.7 [49] |
| $e_{22}$ | 2.51 | 2.407 ± 0.015 [48], 2.5 [49] |
| $e_{31}$ | 0.21 | 0.328 ± 0.032 [48], 0.2 [49] |
| $e_{33}$ | 1.69 | 1.894 ± 0.054 [48], 1.3 [49] |
| Elastic constant (GPa) | | |
| $C_{11}$ | 190.7 | 198.86 ± 0.033 [48], 203 [49] |
| $C_{12}$ | 58.3 | 54.67 ± 0.04 [48], 53 [49] |
| $C_{13}$ | 62.4 | 67.99 ± 0.55 [48], 75 [49] |
| $C_{14}$ | 13.5 | 7.83 ± 0.02 [48], 9 [49] |
| $C_{33}$ | 220.0 | 234.18 ± 0.75 [48], 245 [49] |
| $C_{44}$ | 49.2 | 59.85 ± 0.01 [48], 60 [49] |
| Dielectric constant | | |
| $\varepsilon_{11}$ | 40.6 | 44.9 ± 0.4 [48], 44 [49] |
| $\varepsilon_{33}$ | 24.1 | 26.7 ± 0.3 [48], 29 [49] |

**Table 1.** Piezoelectric constant, elastic constant, and dielectric constant calculated by DFPT and experimentally measured values.

| Decomposed $e_{33}'$ (C/m²) | | | Born effective charge $Z_{33}$ (e) | | | Displacement-response internal-strain constant $\Gamma_{33}$ | | |
|---|---|---|---|---|---|---|---|---|
| Li | Nb | O | Li | Nb | O | Li | Nb | O |
| 0.1 | 0.05 | 0.16 | 1.03 | 6.77 | −2.6 | 0.67 | −0.05 | −0.21 |

**Table 2.** Decomposed piezoelectric constants of $LiNbO_3$.

Thus, Li vacancy is considered to have negligible influence on the piezoelectric properties. Decomposed ionic contribution of piezoelectric strain constant $e_{33}$ is summarized in **Table 2**. Although the Born effective charge of Nb is larger than its formal charge +5e, displacement-response internal-strain constant of Nb is negative value. This indicates that piezoelectricity of $LiNbO_3$ is mainly dominated by displacement of Li. Born effective charge indicates a degree of polarization induced by atomic displacement and dominated by the change in the orbital hybridization. Although anomalously large Born effective charge is crucial for superior piezoelectric properties of perovskite $ABO_3$ materials [50], the present study of decomposition of piezoelectric constant shows that coupling degree between external strain and atomic displacement is also indispensable to understand the piezoelectric properties.

## 6. Piezoelectric properties of perovskite-$LiNbO_3$

Next, we will show how piezoelectric properties are affected by crystal structure, while chemical composition is kept as $LiNbO_3$. Various hypothetical crystal structures common for perovskite-type structure were constructed, and their energetic stabilities were examined by calculating enthalpy $H = U + PV$ ($U$ is total energy obtained by first-principles calculation, $P$ is external pressure, and $V$ is equilibrium volume under pressure $P$) as a function of external pressure. Imposing high pressure is most convenient method to modify crystal structure and find unexpected stable phase. The following eight types of phases were considered:

Cubic, *Pm-3 m*; tetragonal, *P4mm*; and rhombohedral, *R-3 m*.

$LiNbO_3$-ferroelectric phase, *R3c*, and $LiNbO_3$-paraelectric phase, *R-3c*.

Orthorhombic, *Amm2* and *Cmmm*, and high-pressure phase, *P63/m.*

where names of space groups are used to distinguish each structure. Crystal structure of each phase is shown in **Figure 4a**. Polyhedra shown in **Figure 4a** correspond to Nb-centered bonding structure of Nb-O bondings. **Figure 4b** shows the enthalpy difference of each phases as a function of external pressure. Here, external pressure is assumed to be isotropic. Standard of enthalpy was set to be the enthalpy of most stable *R3c* phase under ambient condition. At the positive (compressive) pressure region, $P6_3/m$ phase becomes stable above 21 GPa, which is close to the experimental phase transition pressure of 25 GPa [43]. Details of the phase transition behavior under high pressure are theoretically investigated in our previous work [44]. Unfortunately, $P6_3/m$ phase is highly symmetric and shows no piezoelectricity. At the negative (expansive) pressure region, enthalpy difference becomes smaller as there is an increase of negative pressure except for $R\bar{3}c$ and $P6_3/m$ phases.

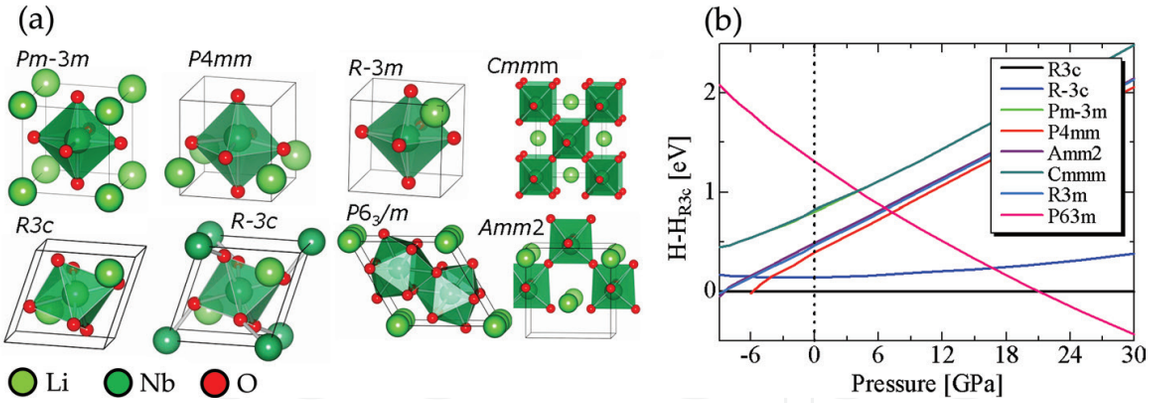



**Figure 4.** (a) Schematic illustration of eight types of perovskite-structured $LiNbO_3$ and their space groups. (b) Enthalpy differences of each phase measured from the enthalpy of *R3c* phase as a function of pressure.

Imposing negative pressure can be achieved by solid solution with parent phase of larger lattice constant. At −6 GPa, *P4mm* phase becomes stable, while *R3m* and *Amm2* phases become stable at −9 GPa. However, bond breaking occurs in Nb-O bonding above −6 GPa for *P4mm* phase. The same bond breaking occurs in *Amm2* and *R3m* phases at −11GPa and −14 GPa, respectively. Thus, those phase transitions occur just before bond breaking.

Within the eight phases shown in **Figure 4a**, only *P4mm*, *R3m*, *R3c*, and *Amm2* phases show piezoelectricity. Piezoelectric stress constant, elastic constant, and dielectric constant of *P4mm*, *R3m*, and *Amm2* phases are compared with those of *R3c* phase in **Table 3**. Various piezoelectric properties are observed by each phase. Especially for *P4mm* and *Amm2* phases, high $e_{33}$ and relatively low $C_{33}$ values are predicted, which are advantageous for large piezoelectric strain constant $d_{33}$. On the other hand, *R3m* phase was found to be unstable because following mechanical stability conditions of rhombohedral symmetry:

$$C_{11}+C_{12}>0, C_{33}>0, (C_{11}+C_{12})^{*}C_{33}>2C_{13}, C_{11}-C_{12}>0, C_{44}>0, (C_{11}-C_{12})^{*}C_{44}>2C_{14} \quad (14)$$

are broken because of $C_{44}<0$.

**Figure 5a** and **b** show piezoelectric properties of *P4mm* phase as a function of pressure and corresponding volume of unit cell. Dotted lines indicate zero pressure states. Piezoelectric stress constant $e_{33}$ of *P4mm* phase shows parabolic behavior and maximum value at zero pressure state. On the other hand, elastic constant $C_{33}$ of *P4mm* phase continuously decreases as volume increases, because orbital hybridization of Nb-O bonding along polarization direction decreases as bond length increases. At the pressure of −6 GPa, $C_{33}$ of *P4mm* phase shows almost zero value. This indicates that Nb-O bonding is broken. Piezoelectric stress constant $d_{33}$ shown in **Figure 5b** increases as volume, because of increase of elastic compliance. Especially at the pressure of −5 GPa just before bond breaking, $d_{33}$ shows maximum value or approximately 1000 pC/N.

This giant piezoelectric constant is almost comparable to that of PZT material [51]. Giant piezoelectric constant is understood as a result of phase instability in morphotropic phase boundary [52]. The same as *P4mm* phase of $LiNbO_3$, we revealed that ZnO also showed anomalously large piezoelectric constant just before phase transition [30].

| | *R3c* | *P4mm* | *R3m* | *Amm2* |
|---|---|---|---|---|
| Piezoelectric stress constant ($C/m^2$) | | | | |
| $e_{15}$ | 3. 73 | 1.14 | 5.10 | 0.64 |
| $e_{22}$ | 2.51 | — | 1.19 | — |
| $e_{31}$ | 0.21 | 0.46 | 0.24 | 0.80 |
| $e_{33}$ | 1.69 | 3.28 | 1.92 | 2.99 |
| Elastic constant (GPa) | | | | |
| $C_{11}$ | 190.7 | 297.2 | 203.0 | 321.8 |
| $C_{12}$ | 58.3 | 48.9 | 169.0 | 91.6 |
| $C_{13}$ | 62.4 | 77.7 | 90.6 | 92.8 |
| $C_{14}$ | 13.5 | — | −42.1 | — |
| $C_{33}$ | 220.0 | 157.7 | 206.6 | 176.4 |
| $C_{44}$ | 49.2 | 39.5 | −29.6 | 32.5 |
| Dielectric constant | | | | |
| $\varepsilon_{11}$ | 40.6 | 56.2 | 36.6 | 28.2 |
| $\varepsilon_{33}$ | 24.1 | 12.3 | 16.2 | 13.3 |

**Table 3.** Piezoelectric constant, elastic constant, and dielectric constant of ***R3c***, ***P4mm***, ***R3m***, and ***Amm2*** phases calculated by DFPT.

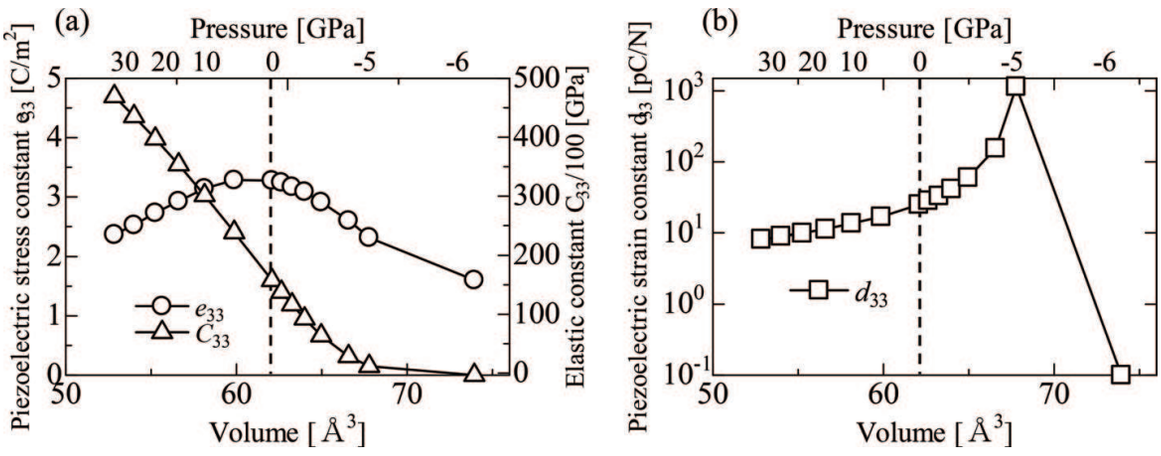



**Figure 5.** (a) Piezoelectric stress constant $e_{33}$ and elastic constant $C_{33}$ and (b) piezoelectric strain constant $d_{33}$ of *P4mm* phase as a function of pressure and corresponding volume of unit cell.

Finally, we would like to show phase transition path between cubic perovskite structure and $LiNbO_3$ structure. **Figure 6a** shows the energy change of *Pm3m* phase as a function of Li displacement along <001>, <011>, and <111> directions. *Pm3m* phase is paraelectric phase. Because ferroelectricity and piezoelectricity of $LiNbO_3$ are dominated by off-centering and displacement of Li, respectively, phase transition from *Pm3m* phase is also expected to be occurred by

Li displacement. Li displacement along <001>, <011>, and <111> directions induces tetragonal, orthorhombic, and rhombohedral phase transition from cubic phase. **Figure 6a** clearly shows that tetragonal phase transition from *Pm3m* phase to *P4mm* phase is the most energetically advantageous. **Figure 6b** shows the phonon dispersion curve of cubic *Pm3m* phase of $LiNbO_3$. Horizontal axis corresponds to sampling path along high symmetric reciprocal point (*q*-point). Within the whole Brillouin zone of reciprocal space, unstable phonon modes with imaginary phonon frequencies are observed. Here, imaginary phonon frequency is represented as negative value for convenience. Therefore, cubic *Pm3m* phase of $LiNbO_3$ is thermodynamically unstable and considered to show phase transition in accordance with specific phonon mode of imaginary frequency (referred as soft mode). Thus, modulated structures were constructed by imposing atomic displacement along normal modes at each symmetric *q*-points. Modulated structures were structurally relaxed, and their space group and energy change from cubic *P4mm* phase were investigated. Summary of such modulated structures are shown in **Table 4**. At Γ point, tetragonal phase transition along with $\Gamma_{15}$ soft mode of cubic phase shown in **Figure 3b** shows energy gain of −0.422 eV/formula unit (f.u.). On the other hand, it was found that modulation at R point gives more stable energy gain of −0.682 eV/f.u. In this case, $R_{25}$ soft mode induces phase transition from cubic *Pm3m* phase to $R\bar{3}c$ phase shown in **Figure 2b**.

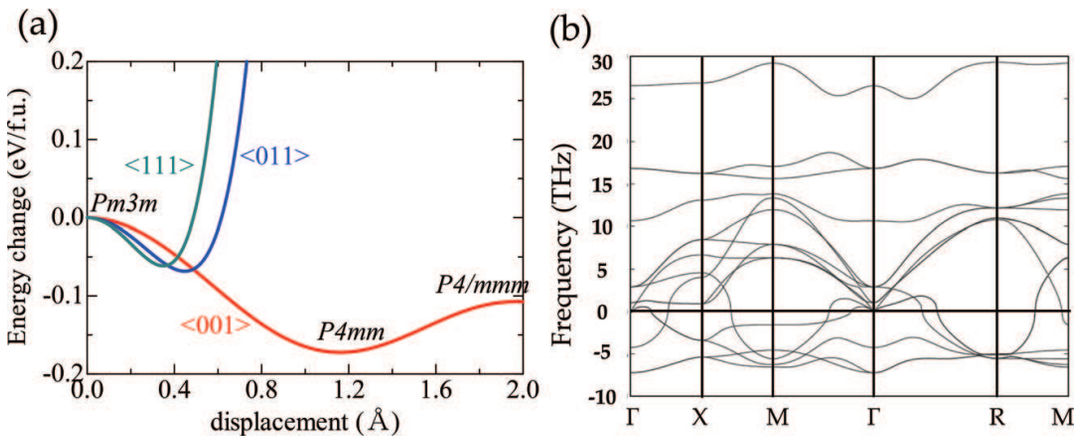



**Figure 6.** (a) Energy change of *Pm3m* phase as a function of li displacement along <001>, <011>, and <111> directions. (b) Phonon dispersion curve of *Pm3m* phase.

| *q*-point | Frequency (THz) | Structure | Space group | Energy gain (eV/f.u.) |
|---|---|---|---|---|
| Γ | −7.22 | Tetragonal | *P4mm* | −0.422 |
| X | −5.38 | Orthorhombic | *Pmma* | −0.220 |
| M | −6.56 | Orthorhombic | *Pmma* | −0.125 |
| R | −5.51 | Rhombohedral | *R-3c* | −0.682 |

"Structure" indicates Bravais lattice of modulated structure from *P4mm* phase. Space group of the relaxed modulated structure and energy gain is also shown.

**Table 4.** Summary of imaginary phonon frequency at each symmetric *q*-point in ***P4mm*** phase of $LiNbO_3$ and corresponding structural phase transition.

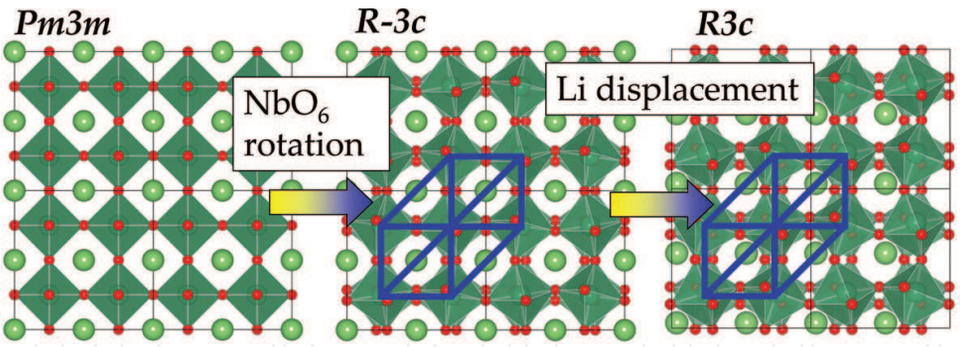



**Figure 7.** Phase transition path between cubic perovskite structure (*Pm3m*) and $LiNbO_3$-structure. Unit cell of $LiNbO_3$ is enclosed with blue lines.

**Figure 7** shows schematic illustration of phase transition mechanism from cubic perovskite structure to $LiNbO_3$ structure. On the contrary to the result of **Figure 6a**, $R_{25}$ soft mode is represented as rotation of $NbO_6$ polyhedra. Then, $\Gamma_{15}$ soft mode of $R\bar{3}c$ phase leads *R3c* phase, which is ground state of $LiNbO_3$. Although the present study shows that perovskite-structured $LiNbO_3$ is thermodynamically unstable while its piezoelectricity is excellent, it can be possible to control phase transition behavior by dopant substitution.

## 7. Summary and conclusion

In this chapter, we briefly introduced sophisticated method of density functional perturbation theory. DFPT can effectively calculate the second derivative of the total energy with respect to the atomic displacement within the framework of first-principles calculation. By using DFPT method, we can predict piezoelectric constants, dielectric constants, elastic constants, and phonon dispersion relationship of any given crystal structure. Moreover, we showed our established computational technique to decompose piezoelectric constants into each atomic contribution, which enable us to gain deeper insights to understand the piezoelectricity of material. By using $LiNbO_3$ as a model material, we showed the predictability of DFPT for piezoelectric properties. In addition, we showed that superior piezoelectric properties are hidden in perovskite-structured $LiNbO_3$. Structural relationship and possible phase transition path between $LiNbO_3$ structure and perovskite structure were discussed and concluded that perovskite-structured $LiNbO_3$ is thermodynamically unstable. Further studies are expected to control relative phase stability between perovskite and $LiNbO_3$ structure by dopant substation and solid solution.

## Author details

Kaoru Nakamura*, Sadao Higuchi and Toshiharu Ohnuma

*Address all correspondence to: n-kaoru@criepi.denken.or.jp

Central Research Institute of Electric Power Industry, Japan

## References

[1] Martin Richard M. Piezoelectricity. Physical Review B. 1972;**5**:1607-1613. DOI: 10.1103/PhysRevB.5.1607

[2] Hohenberg P, Kohn W. Inhomogeneous electron gas. Physics Review. 1964;**136**:B864-B871. DOI: 10.1103/PhysRev.136.B864

[3] Kohn W, Sham LJ. Self-consistent equations including exchange and correlation effects. Physical Review. 1965;**140**:A1133-A1138. DOI: 10.1103/PhysRev.140.A1133

[4] King-Smith RD, Vanderbilt D. Theory of polarization of crystalline solids. Physical Review B. 1993;**47**:1651-1654. DOI: 10.1103/PhysRevB.47.1651

[5] Baroni S, Giannozzi P, Testa A. Green's-function approach to linear response in solids. Physical Review Letters. 1987;**58**:1861-1864. DOI: 10.1103/PhysRevLett.58.1861

[6] de Gironcoli S, Baroni S, Resta R. Piezoelectric properties of III-V semiconductors from first-principles linear-response theory. Physical Review Letters. 1989;**62**:2853-2856. DOI: 10.1103/PhysRevLett.62.2853

[7] Giannozzi P, de GS, Pavone P, Baroni S. Ab initio calculation of phonon dispersions in semiconductors. Physical Review B. 1991;**43**:7231-7242. DOI: 10.1103/PhysRevB.43.7231

[8] Gonze X. Perturbation expansion of variational principles at arbitrary order. Physical Review A. 1995;**52**:1096-1095. DOI: 10.1103/PhysRevA.52.1086

[9] Gonze X. First-principles responses of solids to atomic displacements and homogeneous electric fields: Implementation of a conjugate-gradient algorithm. Physical Review B. 1997;**55**:10337-10354. DOI: 10.1103/PhysRevB.55.10337

[10] Gonze X, Lee C. Dynamical matrices, born effective charges, dielectric permittivity tensors, and interatomic force constants from density-functional perturbation theory. Physical Review B. 1997;**55**:10355-10368. DOI: 10.1103/PhysRevB.55.10355

[11] Baroni S, de GS, Corso AD, Giannozzi P. Phonons and related crystal properties from density-functional perturbation theory. Reviews of Modern Physics. 2001;**73**:515-562. DOI: 10.1103/RevModPhys.73.515

[12] Sághi-Szabó G, Cohen RE. First-principles study of piezoelectricity in $PbTiO_3$. Physical Review Letters. 1998;**80**:4321-4324. DOI: 10.1103/PhysRevLett.80.4321

[13] Sághi-Szabó G, Cohen RE, Krakauer H. First-principles study of piezoelectricity in tetragonal $PbTiO_3$ and $PbZr_{1/2}Ti_{1/2}O_3$. Physical Review B. 1999;**59**:12771-12776. DOI: 10.1103/PhysRevB.59.12771

[14] Ghosez P, Cockayne E, Waghmare UV, Rabe KM. Lattice dynamics of $BaTiO_3$, $PbTiO_3$, and $PbZrO_3$: A comparative first-principles study. Physical Review B. 1999;**60**:836-843. DOI: 10.1103/PhysRevB.60.836

[15] Bellaiche L, Vanderbilt D. Intrinsic piezoelectric response in perovskite alloys: PMN-PT versus PZT. Physical Review Letters. 1999;**83**:1347-1350. DOI: 10.1103/PhysRevLett.83.1347

[16] Bernardini F, Fiorentini V, Vanderbilt D. Spontaneous polarization and piezoelectric constants of III-V nitrides. Physical Review B. 1997;**56**:R10024-R10027. DOI: 10.1103/PhysRevB.56.R10024

[17] Boonchun A, Lambrecht WRL. First-principles study of the elasticity, piezoelectricity, and vibrational styles in $LiGaO_2$ compared with ZnO and GaN. Physical Review B. 2010;**81**:235214. DOI: 10.1103/PhysRevB.81.235214

[18] Karanth D, Fu H. Large electromechanical response in ZnO and its microscopic origin. Physical Review B. 2005;**72**:064116. DOI: 10.1103/PhysRevB.72.064116

[19] Tasnádi F, Alling B, Höglund C, Wingqvist G, Birch J, Hultman L, Abrikosov IA. Origin of the anomalous piezoelectric response in Wurtzite $Sc_xAl_{1-x}N$ alloys. Physical Review Letters. 2010;**104**:137601. DOI: 10.1103/PhysRevLett.104.137601

[20] Al-Yacoub A, Bellaiche L, Wei SH. Piezoelectric coefficients of complex semiconductor alloys from first-principles: The case of $Ga_{1-x}In_xN$. Physical Review Letters. 2002;**89**:057601. DOI: 10.1103/PhysRevLett.89.057601

[21] Armiento R, Kozinsky B, Fornari M, Ceder G. Screening for high-performance piezoelectrics using high-throughput density functional theory. Physical Review B. 2011;**84**:014103. DOI: 10.1103/PhysRevB.84.014103

[22] Akgencab B, Kinacic A, Tassevend C, Cagin T. First-principles calculations on stability and mechanical properties of various $ABO_3$ and their alloys. Materials Chemistry and Physics. 2018;**205**:315-324. DOI: 10.1016/j.matchemphys.2017.11.026

[23] Dai JQ, Song YM, Zhang H. First-principles study of the phonon, dielectric, and piezoelectric response in $Bi_2ZnTiO_6$ supercell. Computational Materials Science. 2015;**101**:227-232. DOI: 10.1016/j.commatsci.2015.01.040

[24] Wan LF, Nishimatsu N, Beckman SP. The structural, dielectric, elastic, and piezoelectric properties of $KNbO_3$ from first-principles methods. Journal of Applied Physics. 2012;**111**:104107. DOI: 10.1063/1.4712052

[25] de Jong M, Chen W, Geerlings H, Asta M, Persson KA. A database to enable discovery and design of piezoelectric materials. Scientific Data. 2015;**2**:150053. DOI: 10.1038/sdata.2015.53

[26] Tinte S, Rabe KM, Vanderbilt D. Anomalous enhancement of tetragonality in $PbTiO_3$ induced by negative pressure. Physical Review B. 2003;**68**:144105. DOI: 10.1103/PhysRevB.68.144105

[27] Wu Z, Cohen RE. Pressure-induced anomalous phase transitions and colossal enhancement of piezoelectricity in $PbTiO_3$. Physical Review Letters. 2005;**95**:037601. DOI: 10.1103/PhysRevLett.95.037601

[28] Shahmirzaee H, Mardani R. Enhancement of piezoelectricity of tetragonal P4mm $SrHfO_3$ under uniaxial stress: A first principle study. Computational Condensed Matter. 2018;**14**:46-48. DOI: 10.1016/j.cocom.2017.12.006

[29] Duan Y, Lv D, Liu K, Wu H, Qin L, Shi L, Tang G. Strain-induced structural, band-structure and piezoelectric evolutions in $Al_{0.5}Ga_{0.5}N$ alloy. Journal of Applied Physics. 2015;**117**:045711. DOI: 10.1063/1.4906779

[30] Nakamura K, Higuchi S, Ohnuma T. Enhancement of piezoelectric constants induced by cation-substitution and two-dimensional strain effects on ZnO predicted by density functional perturbation theory. Journal of Applied Physics. 2016;**119**:114102. DOI: 10.1063/1.4943937

[31] Hamann DR, Wu X, Rabe KM, Vanderbilt D. Metric tensor formulation of strain in density-functional perturbation theory. Physical Review B. 2005;**71**:035117. DOI: 10.1103/PhysRevB.71.035117

[32] Wu X, Vanderbilt D, Hamann DR. Systematic treatment of displacements, strains, and electric fields in density-functional perturbation theory. Physical Review B. 2005;**72**:035105. DOI: 10.1103/PhysRevB.72.035105

[33] Gonze X, Jollet F, Araujo FA, Adams D, Amadon B, Applencourt T, Audouze C, Beuken J-M, Bieder J, Bokhanchuk A, Bousquet E, Bruneval F, Caliste D, Côté M, Dahm F, Da Pieve F, Delaveau M, Di Gennaro M, Dorado B, Espejo C, Geneste G, Genovese L, Gerossier A, Giantomassi M, Gillet Y, Hamann DR, He L, Jomard G, Janssen JL, Le RS, Levitt A, Lherbier A, Liu F, Lukacevic I, Martin A, Martins C, Oliveira MJT, Poncé S, Pouillon Y, Rangel T, Rignanese G-M, Romero AH, Rousseau B, Rubel O, Shukri AA, Stankovski M, Torrent M, Van Setten MJ, Van Troeye B, Verstraete MJ, Waroquier D, Wiktor J, Xue B, Zhou A, Zwanziger JW. Recent developments in the ABINIT software package. Computer Physics Communications. 2016;**205**:106-131. DOI: 10.1016/j.cpc.2016.04.003

[34] Kresse G, Furthmüller J. Efficient iterative schemes for ab initio total-energy calculations using a plane-wave basis set. Physical Review B. 1996;**54**:11169-11186. DOI: 10.1103/PhysRevB.54.11169

[35] Momma K, Izumi F. VESTA: A three-dimensional visualization system for electronic and structural analysis. Journal of Applied Crystallography. 2008;**41**:653-658. DOI: 10.1107/S0021889808012016

[36] Smolenskii GA, Krainik NN, Khuchua NP, Zhdanova VV, Mylnikova IE. The curie temperature of $LiNbO_3$. Physica Status Solidi B. 1966;**13**:309-314. DOI: 10.1002/pssb.19660130202

[37] Karapetyan KG, Kteyan AA, Vardanyan RA. Thermal reduction effect on curie temperature of $LiNbO_3$ ferroelectrics. Solid State Communications. 2006;**140**:474-476. DOI: 10.1016/j.ssc.2006.08.045

[38] Inaguma Y, Yoshida M, Tsuchiya T, Aimi A, Tanaka K, Katsumata T, Mori D. High-pressure synthesis of novel lithium niobate-type oxides. Journal of Physics Conference Series. 2010;**215**:012131. DOI: 10.1088/1742-6596/215/1/012131

[39] Inaguma Y, Yoshida M, Katsumata T. A polar oxide $ZnSnO_3$ with a $LiNbO_3$-type structure. Journal of the American Chemical Society. 2008;**130**:6704-6705. DOI: 10.1021/ja801843v

[40] Nakayama M, Nogami M, Yoshida M, Katsumata T, Inaguma Y. First-principles studies on novel polar oxide $ZnSnO_3$; pressure-induced phase transition and electric properties. Advanced Materials. 2010;**22**:2579-2582. DOI: 10.1002/adma.200903432

[41] Kuno Y, Tassel C, Fujita K, Batuk D, Abakumov AM, Shitara K, Kuwabara A, Moriwake H, Watabe D, Ritter C, Brown CM, Yamamoto T, Takeiri F, Abe R, Kobayashi Y, Tanaka K, Kageyama H. $ZnTaO_2N$: Stabilized high-temperature $LiNbO_3$-type structure. Journal of the American Chemical Society. 2016;**138**:15950-15955. DOI: 10.1021/jacs.6b08635

[42] Katsumata T, Ohba C, Tobe A, Takeda A, Shoji M, Aimi A, Mori D, Inaguma Y. Synthesis of new $LiNbO_3$-type oxynitrides, $Mn(Mn_{1/6}Ta_{5/6})O_{2.5}N_{0.5}$ under high pressure and at high temperature. Chemistry Letters. 2018;**47**:37-39. DOI: 10.1246/cl.170851

[43] Nakamura K, Higuchi S, Ohnuma T. First-principles investigation of pressure-induced phase transition in $LiNbO_3$. Journal of Applied Physics. 2012;**111**:033522. DOI: 10.1063/1.3682522

[44] Mukaide T, Yagi T, Miyajima N, Kondo T, Sata N. High pressure and high temperature phase transformations in $LiNbO_3$. Journal of Applied Physics. 2003;**93**:3582-3858. DOI: 10.1063/1.1556570

[45] Blöch PE. Projector augmented-wave method. Physical Review B. 1994;**50**:17953-17979. DOI: 10.1103/PhysRevB.50.17953

[46] Perdew JP, Ruzsinszky A, Csonka GI, Vydrov OA, Scuseria GE, Constantin LA, Zhou X, Burke K. Restoring the density-gradient expansion for exchange in solids and surfaces. Physics Review Letters. 2008;**100**:136406. DOI: 10.1103/PhysRevLett.100.136406

[47] Togo A, Oba F, Tanaka I. First-principles calculations of the ferroelastic transition between rutile-type and $CaCl_2$-type $SiO_2$ at high pressures. Physics Review B. 2008;**78**:134106. DOI: 10.1103/PhysRevB.78.134106

[48] Kushibiki J, Takanaga I, Arakawa M, Sannomiya T. Accurate measurements of the acoustical physical constants of $LiNbO_3$ and $LiTaO_3$ single crystals. IEEE Transactions on Ultrasonics, Ferroelectrics, and Frequency Control. 1999;**46**:1315-1323. DOI: 10.1109/58.796136

[49] Warner AW, Onoe M, Coquin GA. Determination of elastic and piezoelectric constants for crystals in class (3m). The Journal of the Acoustical Society of America. 1967;**42**:1223-1231. DOI: 10.1121/1.1910709

[50] Ghosez P, Michenaud JP, Gonze X. Dynamical atomic charges: The case of $ABO_3$ compounds. Physical Review B. 1998;**58**:6224-6240. DOI: 10.1103/PhysRevB.58.6224

[51] Kuwata J, Uchino K, Numura S. Dielectric and piezoelectric properties of $0.91Pb(Zn_{1/3}Nb_{2/3})O_3$-$0.09PbTiO_3$ single crystals. Japanese Journal of Applied Physics. 1982;**21**:1298-1301. DOI: 10.1143/JJAP.21.1298

[52] Guo Y, Kakimoto K, Ohsato H. Phase transitional behavior and piezoelectric properties of $(Na_{0.5}K_{0.5})NbO_3$–$LiNbO_3$ ceramics. Applied Physics Letters. 2004;**85**:4121-4123. DOI: 10.1063/1.1813636